Weak Jets and Strong Cyclones: Shallow-Water Modeling of Giant Planet Polar Caps

MORGAN E O'NEILL, KERRY A. EMANUEL, AND GLENN R. FLIERL

Program in Atmospheres, Oceans and Climate, Massachusetts Institute of Technology, Cambridge, Massachusetts

(Manuscript received 16 October 2015, in final form 14 February 2016)

ABSTRACT

Giant planet tropospheres lack a solid, frictional bottom boundary. The troposphere instead smoothly transitions to a denser fluid interior below. However, Saturn exhibits a hot, symmetric cyclone centered directly on each pole, bearing many similarities to terrestrial hurricanes. Transient cyclonic features are observed at Neptune's South Pole as well. The wind-induced surface heat exchange mechanism for tropical cyclones on Earth requires energy flux from a surface, so another mechanism must be responsible for the polar accumulation of cyclonic vorticity on giant planets. Here it is argued that the vortical hot tower mechanism, claimed by Montgomery et al. and others to be essential for tropical cyclone formation, is the key ingredient responsible for Saturn's polar vortices. A 2.5-layer polar shallow-water model, introduced by O'Neill et al., is employed and described in detail. The authors first explore freely evolving behavior and then forced-dissipative behavior. It is demonstrated that local, intense vertical mass fluxes, representing baroclinic moist convective thunderstorms, can become vertically aligned and accumulate cyclonic vorticity at the pole. A scaling is found for the energy density of the model as a function of control parameters. Here it is shown that, for a fixed planetary radius and deformation radius, total energy density is the primary predictor of whether a strong polar vortex forms. Further, multiple very weak jets are formed in simulations that are not conducive to polar cyclones.

1. Introduction

In 2004, the Keck Observatory discovered a warm region situated on Saturn's South Pole (Orton and Yanamandra-Fisher 2005), which implied the presence of a warm-core polar vortex. This discovery was followed in 2007 by infrared imaging of both polar hemispheres by the NASA *Cassini* mission, currently in orbit around Saturn. A surprising result was that both poles exhibited very localized tropospheric hot spots, though in 2007 one pole was receiving constant summer sunlight and the other was not (Fletcher et al. 2008). These hot spots were 6–8 K warmer than fluid that is just 10° from the pole. The warm anomalies extended downward at least as far as the lower limit of the observations at 1 bar. The *Cassini* mission took high-resolution images of the southern hot spot and showed that it was the center of a vast, strong cyclone (Vasavada et al. 2006). Sánchez-Lavega et al. (2006) found a peak tangential velocity of $160 \pm 10 \, \mathrm{m \, s^{-1}}$ at 87° (3000 km from the pole).

In 2006, a second South Polar survey was taken and reported by Dyudina et al. (2009). They identified multiple polar vortex features, including an analog of hurricane eyewalls: the vortex has concentric annuli of tall convective clouds, dropping a shadow over a deep and largely clear, anomalously warm eye. The inner eyewall has a horizontal wavenumber-2 distortion, and the outer wall is azimuthally symmetric with an estimated height of 30–40 km. The South Polar eye itself is consistently the warmest place imaged on the entire planet. Predicted by Fletcher et al. (2008), a very similar hot cyclone has been observed on Saturn's North Pole as well (Baines et al. 2009) and appears even more symmetrical. The polar vortex eyewalls, rapid circular jets, and deep clear eyes are reminiscent of hurricanes; yet the thermodynamic mechanism must be fundamentally different because there is no sea surface[1] below. Nonetheless, there are a remarkable number of similarities between terrestrial hurricanes and Saturn's polar cyclones,

---

Corresponding author address: Morgan E O'Neill, Weizmann Institute of Science, 234 Herzl St., Rehovot 7610001, Israel. E-mail: morgan.oneill@weizmann.ac.il

[1] More precisely, there is no known discontinuity in enthalpy, be it solid or fluid.

detailed thoroughly in Dyudina et al. (2009). Multiple observations of each pole since the cyclones' discovery suggests that they are "present at all epochs" seasonally (Fletcher et al. 2015).

Polar vortices have been observed on Earth, Venus, and Neptune, but they are all transient and cold or only slightly warmer than their immediate surroundings. Saturn's polar cyclones, in contrast, are remarkably steady and hot. Saturn's polar cyclones are the longest-lived cyclones ever observed in the solar system (Jupiter's Great Red Spot is an anticyclone). While Saturn boasts the most comprehensive observations of any giant planet, the range of masses, compositions, and rotation rates of Jupiter, Uranus, and Neptune provide multiple benchmarks for a polar cyclone theory.

In this paper, we expand the work of O'Neill et al. (2015, hereafter OEF), which proposes a predictive theory for polar cyclones on giant planets. In section 2, we provide a literature review of relevant terrestrial tropical cyclone theory and describe its potential for application to gas giants. The details of the shallow-water model used are described in sections 3 and 4. In section 5, results are provided from freely decaying single-storm simulations to confirm that the model can reproduce well understood single-vortex behavior. Section 6 provides a derivation of the governing energy parameter that controls qualitative behavior for both freely decaying and forced-dissipative simulations. Section 7 modifies this energy parameter and describes steady-state behavior for forced-dissipative simulations. Section 8 discusses ambiguity in model interpretation, the model's applicability, and future work. Appendix A provides the model energy equations, and appendix B discusses the domain setup and numerical considerations.

2. Beta drift on Earth and giant planets

The polar cyclone hypothesis proposed in OEF borrows from the understanding of terrestrial tropical cyclones (TCs). TCs in the tropics tend to move westward and poleward because of the varying Coriolis parameter. This motion is called beta drift (Adem 1956) and is due to the nonlinear interaction between a strong cyclone and the vorticity gradient of the background state. This behavior is observed in numerical simulations (e.g., Schecter and Dubin 1999) without any background flow as well as in observations of real hurricanes.

On a spinning planet, a vorticity gradient is provided by the variation of the Coriolis frequency with latitude in a stationary atmosphere. On an f plane, a similar gradient can be achieved if a vortex itself provides the background state. Small, linearized anomalies added to this background state will induce vortex Rossby waves (Melander et al. 1987; Montgomery and Kallenbach 1997), and nonlinear anomalies will additionally experience beta drift. A TC is a natural laboratory for vortex Rossby waves. TCs are small enough that the change in Coriolis parameter f across their diameter is small, but their significant primary circulation can provide a sufficient vorticity gradient to sustain vortex Rossby waves (Montgomery and Kallenbach 1997; Möller and Montgomery 1999; McWilliams et al. 2003) and potentially beta drift.

Anomalies of great interest in the largely symmetric hurricane environment are small but severe thunderstorms. The hurricane community has not resolved the role of local, deep convective thunderstorms in hurricane formation and maintenance. Some authors argue that azimuthally symmetric fluxes over the sea surface are sufficient for hurricane growth (e.g., Emanuel 1986) and that strong eddies are deleterious for intensification [e.g., in the idealized study of Nolan and Grasso (2003)]. Others maintain that deep convective towers pump vorticity into the mean flow (Montgomery et al. 2006; Persing et al. 2013). This latter hypothesis may be relevant to a moist convective giant planet atmosphere. These terrestrial deep convective towers converge high-angular-momentum air at their base, creating a positive vorticity anomaly. Moist air rises rapidly through the cumulonimbus cloud, releases latent heat, and diverges just below the tropopause, leading to a negative vorticity anomaly. Montgomery et al. (2006) contend that these anomalies can react with the environment and strengthen a hurricane by transporting vorticity toward the hurricane eye. Idealized experiments with a basic-state parent vortex confirm that small vortical anomalies are axisymmetrized (Melander et al. 1987) and that positive anomalies indeed merge (e.g., Montgomery et al. 2006; Hendricks et al. 2014). The wind-induced surface heat exchange mechanism, which is an important feedback for the primary energy source of hurricanes, is precluded because there is no surface at the base of giant planet tropospheres.

There is consensus that moist convection is occurring in the weather layers of at least Jupiter and Saturn, and potentially Uranus and Neptune as well (e.g., Gierasch et al. 2000; Vasavada et al. 2006); this may even be the energy source for the jets (Ingersoll et al. 2000; Lian and Showman 2010). For Saturn's South Polar region, Dyudina et al. (2009) measured the mean winds of the surrounding flow as well as the local rotation of many puffy cloudy features that are advected around the vortex. They find that the flow surrounding the vortex is dominated by small anticyclonic vortices advected by the nearly irrotational flow outside the outer eyewall.

OEF assume that a fraction of the anticyclonic vortices in the South Polar region are the tops of tropospheric

convective towers, rooted in or below the water cloud. PV conservation would imply that their anticyclonicity is balanced by a cyclonic anomaly near the cloud base, which may react to the Coriolis gradient of the planet and move upgradient, or poleward. Over time, a large-enough poleward flux of cyclonic vorticity may be sufficient to create and maintain a polar cyclone. Baines et al. (2009) speculate that the small cloud features may deliver energy to the North Polar cyclone on Saturn, if they are indeed of moist convective origin, though they did not provide a mechanism. Other authors (e.g., Ingersoll et al. 2000) have envisioned exactly this mechanism for the jets but not for the polar cyclones. We find that beta drift of sufficient cyclonic vorticity can drive an equivalent-barotropic polar cyclone without the need for a frictional surface.

A few idealized modeling studies and laboratory experiments have specifically studied the dynamics of giant planets' thin weather layers. They provide evidence that the drift of small positive anomalies is indeed sufficient to create a polar cyclone. Scott (2011) employed a polar beta plane to study the motion of patches of cyclones and anticyclones on a pole. His quasigeostrophic (QG) single-layer simulations demonstrate the genesis of a circumpolar cyclone due to beta drift. The cyclone tends to orbit the pole in equilibrium, strongly mixing the rest of the fluid in the polar cap. Scott and Polvani (2007) use a forced-dissipative model with full spherical geometry and find a polar cyclone that swims around the pole, constrained by the poleward-most jet. Schneider and Liu (2009) and Liu and Schneider (2010) also find a broad polar cyclone that precesses around the pole in a spherical shell that extends in pressure to 3 bars. The model used in the present work is the first to force a polar domain with small thermal perturbations that mimic observed moist convection in size, strength, and duration, motivated by abundant observations of intense moist convection on the gas giants (Little et al. 1999; Gierasch et al. 2000; Li et al. 2004).

3. The model

We use the shallow-water (SW) system as a laboratory for simple, parameterized convection in a thin-shell weather layer. Several aspects of polar dynamics may render the commonly used QG system too restrictive for our purposes. Most notably, the Rossby number of Saturn's polar vortices may be as high as 1 (Dyudina et al. 2009). The Rossby number suggests a cyclone in gradient wind balance, and the QG system is only valid for motions in approximate geostrophic balance. Also, the SW system assumes that the typical fluid height is much smaller than the typical horizontal length scale, $H \ll L$; the QG system goes one step further and assumes that perturbations of the background fluid height are comparatively small, $h' \ll H$. The QG system is inappropriate for oceanic warm-core rings (Flierl 1984) and may also be a poor fit for Saturn' polar vortices, because their centers are the deepest, hottest places observed on the entire planet, representing a significant deviation in geopotential.

We employ a 2.5-layer shallow-water system centered on the pole for this study. The two active layers represent the troposphere, which extends from the base of the water cloud to the temperature inversion that indicates the tropopause. The troposphere is expected to be statically stable and follow a moist adiabat, much like Earth's troposphere. The abyssal layer below the two active layers is a representation of the deep and (possibly) neutrally stable convecting interior.

Since the feature of interest in this study is in the immediate polar region, it is unnecessary to model a spherical shell. On Saturn, which provides the primary motivation for the simulations, the polar caps are enclosed by a jet at 75° in the Southern Hemisphere (Vasavada et al. 2006) and 74° in the Northern Hemisphere, which likely act as strong barriers to mixing (Dritschel and Mcintyre 2008). In this work, we model polar caps and assume that the outer radial limit plays the role of a jet barrier.

The pole is a unique place where the planetary vorticity gradient reaches zero. A traditional beta plane is not appropriate here because of the quadratic nature of the Coriolis frequency. We use the polar beta plane (Leblond 1964; Bridger and Stevens 1980) to approximate the planetary vorticity gradient near the pole. The Coriolis frequency $f = f_0 - \beta r^2$, where $r^2 = x^2 + y^2$, and $\beta = f_0/(2a^2)$ has units of per square meters per second. All sign conventions are consistent with Northern Hemisphere flows to reduce potential confusion; however, we avoid the term "counterclockwise" and only refer to cyclonicity of flows.

Physical forcing and dissipation

OEF (see their methods section) use a baroclinic forcing to drive an equivalent-barotropic polar cyclone. The storm forcing function S_{st} simulates a moist convective environment with localized deep convective towers, which are shaped as truncated Gaussians in space, with a boxcar function for time behavior (stepping from zero to a fixed value over the storm duration and then back to zero). The storms occur in batches. Gravity waves are not strongly triggered because the peak vertical forcing velocity is generally very low. Convection is simulated by locally thinning the lower active layer and thickening the upper active layer immediately above (Fig. 1), as if a storm is fluxing mass from the lower to upper layer. Simultaneously, the layer
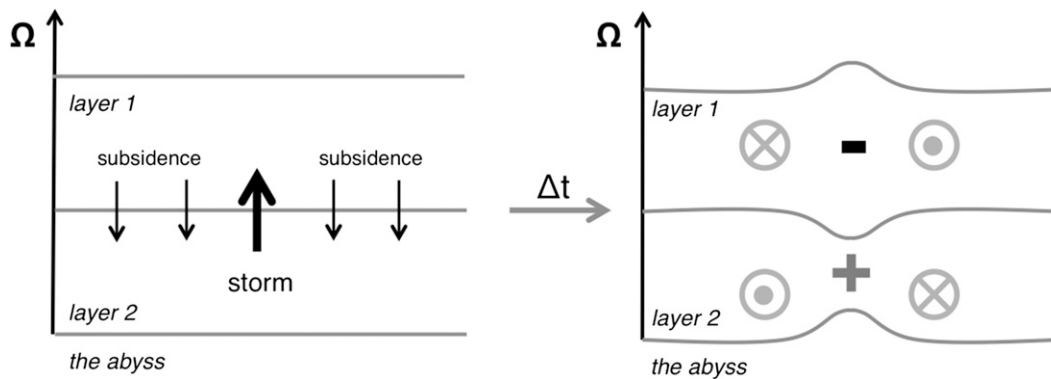
FIG. 1. (left) Mass forcing scheme. (right) After the transient mass forcing (typically a fraction of a day), the flow approaches geostrophic balance by establishing a baroclinic dipole in the vertical.

interface is everywhere else slightly and uniformly raised to conserve layer mass at each time step and represent subsidence.[2] Of course, this forcing is actually dry, but the vertical velocities and areal extents of the convecting regions parameterize the behavior of a moist, statically stable atmosphere. This forcing adds available potential energy (APE), which can convert to kinetic energy (KE) as motions approach geostrophic balance. See Showman (2007, hereafter S07) for a very similar forcing for 1.5-layer midlatitude simulations of Jupiter [other examples are Li et al. (2004) and Smith (2004)].

An additional degree of freedom that we do not add to this model is the ability of storms to advect according to some appropriately weighted mean wind speed *while* they grow. One could argue that deeply rooted storms either move negligibly during their brief active lifespan or move with the upper winds of the neutrally buoyant abyssal layer (which would have an independent streamfunction that we do not provide in this model). In any case, fixing the storm location has not impeded the potential for polar cyclogenesis in our simulations, so that advance is left for future work.

In this model, there is no large-scale forcing in the momentum equations. There is also only minimal numerical dissipation in order to more realistically simulate an essentially inviscid weather layer. See appendix B for a description of numerical friction and hyperviscosity for stability. Radiative relaxation is the only large-scale energy removal in the model [as in S07 and Scott and Polvani (2008)], and it removes APE by damping

thickness perturbations. The estimated radiative time scale τ_{rad} on Saturn is quite high; approximately 9 Earth years (Conrath et al. 1990). To reduce computational expense, values used in this study range from 150 to 400 days, but still $\tau_{rad} \gg \tau_{st}$, where τ_{st} is the storm lifetime. The radiative time scale is the same for each layer. This last choice is more for simplicity than based on physical intuition, and future work should explore more complicated layer radiative functions.

This thermal damping is more physically motivated on giant planets than energy removal by mechanical damping of the winds. For example, hypoviscosity, with no clear physical interpretation, has been used by Scott and Polvani (2007); they also consider linear Rayleigh drag. Liu and Schneider (2010, 2011) and Schneider and Liu (2009) also use Rayleigh drag. In those papers, the stated motivation for linear drag is the cumulative effect of magnetohydrodynamic drag that occurs much deeper.

As in OEF, our 2.5-layer model assumes an inert, abyssal bottom layer, which rules out a barotropic mode [see Achterberg and Ingersoll (1989) for a normal-mode QG model that allows an abyssal flow and therefore a barotropic mode]. Because the system is nonlinear and divergent, the baroclinic modes are coupled, and a sum of modal energies will not include the energy in gravity waves; yet they provide us with more physically relevant deformation radii. We normalize lengths in our model by the internal deformation radius L_{D2}.

4. Nondimensional system

Nondimensionalization in textbooks and well-behaved physical models commonly involves a velocity scaling to arrive at a Rossby number or a Froude number. In such cases, it is appropriate to fix nondimensional parameters in this way, because the system is further constrained by a forcing chosen in

---

[2] Downdrafts in the vicinity of deep convection may be similarly localized and nearly as intense as others have found in observations (Gierasch et al. 2000) and Jovian simulations (Lian and Showman 2010). We omit that complexity here, assuming instead a constant subsidence in the remainder of the domain. This may be a particularly poor assumption for the polar region, where the deformation radius reaches a minimum and may confine downdrafts.

TABLE 1. Nondimensional parameters and their definitions. Note that L_{D2} is the second baroclinic deformation radius, equal to the second baroclinic gravity wave speed c_{e2} divided by f_0.

Symbol	Parameter	Range	Meaning
$\tilde{c}_1^2$	c_1^2/c_{e2}^2	4–10	Scaled first-layer GW speed
$\tilde{c}_2^2$	c_1^2/c_{e2}^2	3–9	Scaled second-layer GW speed
H_1/H_2	—	0.5–1.5	Vertical aspect ratio
Br_2	L_{D2}^2/R_{st}^2	0.25–4	Second baroclinic Burger number
$\tilde{\beta}$	$L_{D2}^2/(2a^2)$	25	Scaled β
Ro_{conv}	$W_{st}/(H_1 f_0)$	2×10^{-5}–2×10^{-2}	Convective Rossby number
ρ_1/ρ_2	—	0.95	Layer stratification
$\tilde{\tau}_{st}$	$\tau_{st} f_0$	2–15	Scaled storm duration
$\tilde{\tau}_{stper}$	$\tau_{stper} f_0$	$1\tilde{\tau}_{st}$–$4\tilde{\tau}_{st}$	Scaled storm period
$\tilde{\tau}_{rad}$	$\tau_{rad} f_0$	$33\tilde{\tau}_{st}$–$1.3 \times 10^3 \tilde{\tau}_{st}$	Scaled radiative time scale
#	—	1–822	Simultaneous storm number
Re	$c_{e2} L_{D2}^3/\nu$	5×10^4	Reynolds number
Pe	$c_{e2} L_{D2}/\kappa$	1×10^5	Peclet number

advance to result in particular behavior. However, we want to avoid scaling that assumes a "typical" horizontal velocity. It is possible that this system will demonstrate different flow regimes in its very large parameter space, and we do not know a priori even the order of magnitude of typical velocities in the system. Therefore, the system is scaled by functions of the control parameters only, and we consider the Rossby and Froude numbers to be descriptions of the behavior at statistical equilibrium. We still can define a convective Rossby number, $Ro_{conv} = W_{st}/(f_0 H_1)$ (Kaspi et al. 2009), since its components are all control parameters, but this should not be confused with the global Rossby number that results from horizontal velocity and length scales. The 13 nondimensional parameters are listed in Table 1. The upper- and lower-layer thicknesses are H_1 and H_2, respectively; R_{st} is the dimensional storm radius; a is the dimensional planetary radius; W_{st} is the dimensional peak vertical velocity of the convective mass flux; τ_{st} is the dimensional storm lifetime; τ_{stper} is the dimensional time between the beginning of one batch of storms and the next batch such that $\tau_{stper} - \tau_{st}$ is the duration between the end of one batch and the beginning of the next; and τ_{rad} is the dimensional radiative relaxation time scale. Table 1 is reproduced here, in part from the supplementary information in OEF.

The Burger number appears in the forcing term because the specified storm radius is an additional length scale. The stratification parameter ρ_1/ρ_2 and number of storms forced simultaneously # remain the same since they were nondimensional to begin with. We normalize horizontal lengths by L_{D2}, thicknesses by H_1, and time by f_0^{-1}. The model solves for layer velocities and heights at each time step. Subscripts 1 and 2 refer to the upper and lower layers, respectively. Our nondimensional shallow-water system is

$$\frac{\partial \mathbf{u}_1}{\partial t} = -(1 - \tilde{\beta}\mathbf{x}^2 + \zeta_1)\hat{\mathbf{k}} \times \mathbf{u}_1$$
$$- \nabla \left(\tilde{c}_1^2 h_1 + \tilde{c}_2^2 h_2 + \frac{1}{2}|\mathbf{u}_1|^2 \right) - Re^{-1}\nabla^4 \mathbf{u}_1, \quad (1)$$

$$\frac{\partial \mathbf{u}_2}{\partial t} = -(1 - \tilde{\beta}\mathbf{x}^2 + \zeta_2)\hat{\mathbf{k}} \times \mathbf{u}_2$$
$$- \nabla \left(\gamma\tilde{c}_1^2 h_1 + \tilde{c}_2^2 h_2 + \frac{1}{2}|\mathbf{u}_2|^2 \right) - Re^{-1}\nabla^4 \mathbf{u}_2, \quad (2)$$

$$\frac{\partial h_1}{\partial t} = -\nabla \cdot (\mathbf{u}_1 h_1) + S_{st} - \frac{h_1 - 1}{\tilde{t}_{rad}} + Pe^{-1}\nabla^2 h_1, \quad (3)$$

$$\frac{\partial h_2}{\partial t} = -\nabla \cdot (\mathbf{u}_2 h_2) - \frac{H_1}{H_2} S_{st} - \frac{h_2 - 1}{\tilde{t}_{rad}} + Pe^{-1}\nabla^2 h_2, \quad (4)$$

$$S_{st} = \begin{cases} \left[\sum_{j=1}^{\#} Ro_{conv} \exp\left[-B_{r2}\frac{(\mathbf{x} - \mathbf{x}_j)^2}{0.36} \right] \right] + subsidence, & \text{if} \quad \tilde{t}_{clock} \leq \tilde{\tau}_{st} \\ 0, & \text{if} \quad \tilde{\tau}_{st} < \tilde{t}_{clock} \leq \tilde{\tau}_{stper} \end{cases} \quad (5)$$

for a $\tilde{t}_{clock}$ that resets to zero every time it equals $\tilde{\tau}_{stper}$. The γ term is equal to $(\rho_1/\rho_2)(\tilde{c}_2^2/\tilde{c}_1^2)(H_1/H_2)$ (Simonnet et al. 2003). The factor of 0.36 in the denominator of the Gaussian exponent adjusts the vortex width such that R_{st}
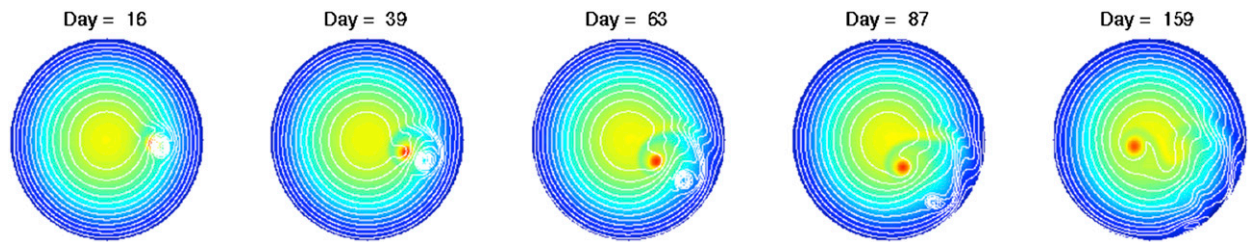
FIG. 2. Case of a single, strong baroclinic storm. The white contours indicate upper-layer potential vorticity; the maximum is at the pole in the center of the domain. The colors indicate lower-layer potential vorticity. A single pulsed storm is vertically sheared, and the upper-layer anticyclone moves equatorward while the lower-layer cyclone moves poleward. In this case, the lower-layer potential vorticity maximum is at the center of the very strong pulsed storm and not at the pole.

is approximately the radius at which the amplitude is $W_{st}/2$ (full-width half-max).

The nondimensional Coriolis parameter $\tilde{\beta}$ provides a measure of the Coriolis gradient with respect to the second baroclinic deformation radius L_{D2} in the nondimensional model. For constant f_0, a planet with large $\tilde{\beta} = L_{D2}^2/(2a^2)$ will have small values of a/L_{D2}: around 20 or 30. A planet with small $\tilde{\beta}$ has $a/L_{D2} \gtrsim 40$. In this paper, we generally use a/L_{D2} for ease of interpretation.

5. Freely evolving, single-storm simulations

The first set of experiments explores freely evolving flows, wherein one storm is initially forced and then allowed to decay. These experiments serve to benchmark the model and confirm predictable behavior. The background state has zero mean flow, for both these experiments and the forced-dissipative set in following sections. For these decaying experiments in particular, a zero background flow allows us to isolate the nonlinear dynamics due to the vortex only, as in Chan and Williams (1987). No radiative relaxation is imposed. The storms decay more quickly than they would in a real, nearly inviscid atmosphere, but slowly enough to observe the nonlinear interaction with the planetary vorticity gradient.

When a single equivalent-barotropic cyclone is initially forced and then allowed to evolve, it induces a Rossby wave by wrapping high-PV fluid from the pole to its west and low-PV fluid from more equatorward regions to its east. For sufficiently strong cyclones, this happens quickly and nonlinearly, and creates β gyres (Chan and Williams 1987) that also propel the cyclone poleward. The inverse case occurs for anticyclonic vortices: a Rossby wave always forms, and the strongest anticyclones self-advect equatorward.

In the case of a single, strong baroclinic storm, in which an anticyclone sits exactly above a cyclone, the stack begins to shear apart immediately after the brief forcing period ends (Fig. 2). In the lower layer, the cyclone moves poleward. Low-PV air [relative vorticity

$\xi < f(r)$], which is wrapped around and poleward of the strong cyclone, moves directly over the pole as the cyclone moves poleward. The low-PV air remains there unless or until the cyclone itself makes it to the pole. This can be seen in Fig. 2; as the cyclone advects high-PV air equatorward, the highest-latitude region entrains low-PV air. Meanwhile, the anticyclone moves toward the equatorward boundary. In both cases, each layer's vortex begins to spin up a vertically aligned like-signed vortex in the opposite layer.

Energy transfer and vertical alignment

Our simulated storms are baroclinic. When a single storm is initially forced and allowed to evolve freely, the anomaly in each layer reacts with the local Coriolis gradient, and each layer evolves nearly independently of the other for early times. However, a vertical energy cascade to the gravest mode (which, in this simple system, is just from the second to the first baroclinic mode) begins almost immediately and results in increasing vertical alignment of the flow. This is the mechanism by which baroclinic storm forcing can ultimately force equivalent-barotropic cyclones [see Polvani (1991) for an exploration of vertical vortex–vortex alignment] and is more efficient for higher local Coriolis gradient (Venaille et al. 2012). Its effect can be seen in Fig. 3.

In Fig. 3, the contours measure the magnitude of the equivalent barotropic component of the fluid and would not appear for purely baroclinic motions. We can see that the lower-level cyclone is able to spin up more upper-layer fluid, more quickly, than its counterpart on the large planet because of its higher Coriolis gradient. We can also see that, while the cyclone moves poleward on the small a/L_{D2} planet, it temporarily advects negative PV fluid over the pole in both layers before it reaches the pole. The cyclone on the large a/L_{D2} planet has the same size and intensity but is unable to self-advect a significant distance poleward because of a significantly weaker beta drift effect. Nonetheless, nonlinear effects can still be seen in the advection of low-PV air poleward
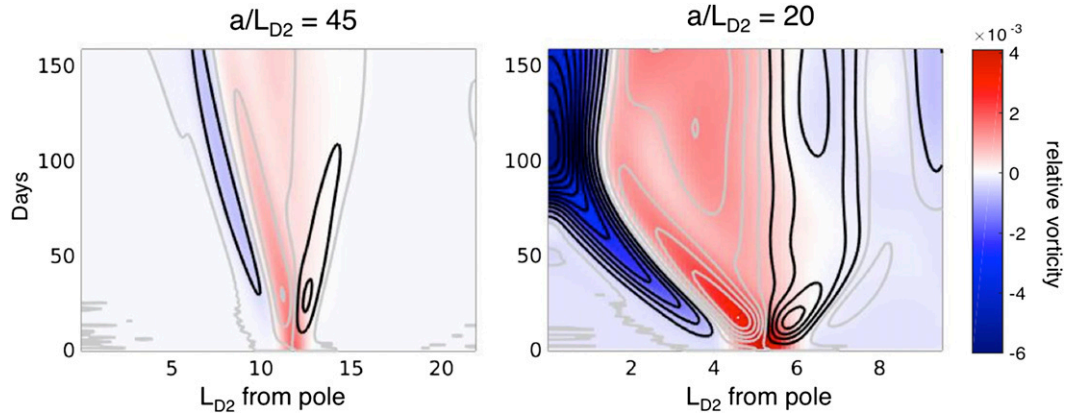
FIG. 3. Vertical alignment of the fluid is faster and more effective for larger beta. The colors show the azimuthally averaged perturbation PV $\langle q'_2 \rangle$ of the lower layer, where a cyclonic storm is initialized—on (left) a small-$\hat{\beta}$ (large a/L_{D2}) planet and (right) a large-$\hat{\beta}$ (small a/L_{D2}) planet. White is $\langle q'_2 \rangle = 0$, and red colors denote positive perturbation PV. Gray contours indicate positive and black contours indicate negative depth-integrated perturbation PV. The contour intervals are the same for each graph, denoting an increase or decrease of 5×10^{-4}. Not shown is the anticyclone that forms in the upper layer. The depth integration shown by the contours indicates the extent to which the vorticity is vertically aligned; for a purely second baroclinic structure, the depth integration would be zero.

of the original cyclone. Strong storms on small a/L_{D2} planets appear the most promising candidates for polar cyclone forcing, and the forthcoming forced-dissipative experiments suggest that strong vortex–vortex interaction does not change this outcome.

6. Deriving an energy parameter

In the course of running hundreds of simulations, we found that increasing any parameter that increases energy density has a similar impact on the qualitative nature of the equilibrium flow. Energy density (depth-integrated total energy per L_{D2}^2) seems to be a governing parameter for the flow. Therefore, it would be convenient to be able to predict the energy density as a function of control parameters without having to run the simulation for every single parameter combination.

S07 derives an "energy parameter" that scales as the equilibrated APE value. We generalize this parameter to our 2.5-layer model with variable stratification and layer thicknesses for our particular constraint of instantaneous mass conservation in each layer (O'Neill 2015). In this section, an energy parameter E_p is derived for the single-storm experiments described above, and in section 7 it is modulated for forced-dissipative simulations.

The available potential energy induced by one storm A_{st} affects the entire domain as a result of mass-conserving subsidence outside of the storm environment. To find a scaling for A_{st}, we first look at the modified height fields in each layer. The top layer experiences an increase in thickness Δh_{1st} within the boundaries of the storm; and the rest of the domain experiences constant subsidence Δh_{1sub}.

The thickness perturbation due to one storm, over the area of the storm, scales as

$$\Delta h_{1st} = \text{Ro}_{conv} \tilde{\tau}_{st} \quad \text{and} \tag{6}$$

$$\Delta h_{2st} = -\frac{H_1}{H_2} \Delta h_{1st}. \tag{7}$$

The areal fraction covered by one storm a_r is a function of the Burger number:

$$a_r = \frac{\pi}{\text{Br}_2 L_{dom}^2}. \tag{8}$$

This expression neglects the Gaussian shape of the storms and instead assumes cylinders or "top hats" with a radius equal to the location of its full-width at half-maximum amplitude of the vortex). This approximation should introduce a negligible error in the energy scale.

An additional source or sink of APE can come from the subsiding regions in the rest of the domain $(1 - a_r)$. The domain-wide storm forcing and subsidence are not necessarily a source of APE at any given instant. APE is only increased where Δh_i is the same sign as h'_i. In this instance of a single storm being initialized as thickness perturbations to two otherwise quiescent layers, the entire domain contributes APE.

Because of layer mass conservation, imposed at every time step, the total volume of the storm forcing is always equal to the total volume of the subsidence elsewhere in the domain. We can relate a perturbation thickness due to subsidence to the perturbation thickness due to storms:

$$\Delta h_{i\text{sub}} = -\frac{a_r}{1 - a_r} \Delta h_{i\text{st}}. \qquad (9)$$

To find a scale A_{sc} for the APE of the entire domain, we consider the contributions from both the storm and subsidence regions, using the above substitutions to express each height in terms of $\Delta h_{1\text{st}}$:

$$\int_{\text{storm}} A_{sc} dA_r = a_r \left[\frac{1}{2} \frac{\rho_1}{\rho_2} \frac{H_1}{H_2} \tilde{c}_1^2 \Delta h_{1\text{st}}^2 \right.$$
$$\left. + \frac{1}{2} \tilde{c}_2^2 \left(\frac{H_1}{H_2} \right)^2 \Delta h_{1\text{st}}^2 - \gamma \tilde{c}_1^2 \frac{H_1}{H_2} \Delta h_{1\text{st}}^2 \right]. \quad (10)$$

Summing these contributions yields A_{sc} as a function of our scaled $\Delta h_{1\text{st}}$ and other nondimensional parameters, which we designate as E_p:

$$E_p = \left(\frac{1}{2} \frac{\rho_1}{\rho_2} \tilde{c}_1^2 + \frac{1}{2} \frac{H_1}{H_2} \tilde{c}_2^2 - \gamma \tilde{c}_1^2 \right) \frac{H_1}{H_2} (\text{Ro}_{\text{conv}} \tilde{\tau}_{\text{st}})^2 \left(\frac{a_r}{1 - a_r} \right).$$
$$(11)$$

It is entirely composed of control parameters and does not require any guess about equilibrium wind speeds. This parameter should scale with the total equilibrated potential energy per deformation radius area L_{D2}^2 of each simulation. The energy parameter is not a function of the hyperviscosity or diffusion parameters, though in reality the model's high dissipation must impact the dynamics to some extent. However, our choice of fixing nondimensional viscosity across the models and consistently resolving L_{D2} allows us to largely ignore this issue, because the impact should then be uniform among the simulations.

A modified E_p

The parameter E_p is evidently a scaling only for potential energy, given its basis in a forcing of height perturbations only. Depending on the nature of the flow at equilibrium for the forced-dissipative cases, it is possible that much of the energy could be in kinetic form. The internal Burger number $\text{Br}_2 = L_{D2}^2 / R_{\text{st}}^2$ can serve as a ratio of potential to kinetic energy. When $\text{Br}_2 > 1$, storms are smaller than L_{D2}, and much of the energy is converted to kinetic energy of horizontal winds. A Burger number less than 1 allows a large storm forcing to maintain interface deviations and store potential energy. Our energy parameter does not include a term for kinetic energy, because Br_2 only appears in E_p as a scaled storm area, without any connection to balanced flow. We can expect that E_p in simulations with large Br_2 overestimates APE, because much of the energy becomes kinetic. This is indeed the case, as shown in Fig. 4. The size of the markers scales linearly with the Burger number, and for the largest
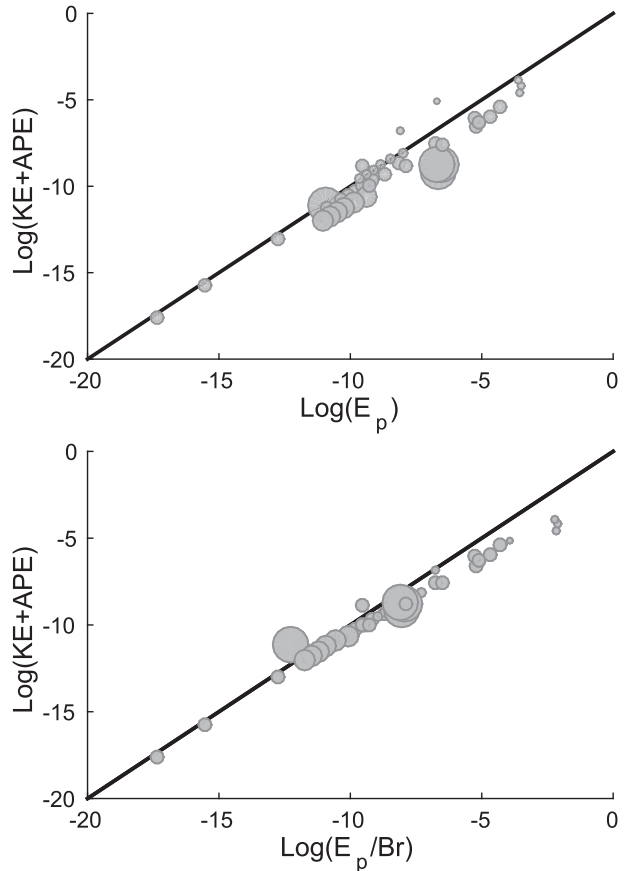

FIG. 4. (top) The energy parameter E_p and (bottom) the modified $\hat{E}_p$, with the 1:1 line for reference. The size of the circle scales linearly with the Burger number; big circles indicate large Burger numbers (small storms). The difference is small, but the correction removes a systematic bias.

Burger number simulations the energy parameter does overestimate APE. To correct the bias, one can divide E_p by the Burger number (black circles in Fig. 4). We define $\hat{E}_p = E_p / \text{Br}_2$ as our primary energy scaling. The rms velocity is also predicted very well by the energy parameter; $U = \sqrt{2\hat{E}_p}$ (O'Neill 2015).

7. Forced-dissipative multistorm simulations

The primary set of experiments constantly forces the model with APE via randomly placed storms[3] and

---

[3] The storms are random in space but not in time. They are either all "on" or all "off." This does cause a sawtooth variation in the total model energy, but it is small, and the steady-state polar cyclones do not exhibit this sawtooth oscillation for short time scales relevant to moist convection. In fact, once a polar cyclone develops, it is difficult to observe small storms at all, because their magnitude and size are much smaller.
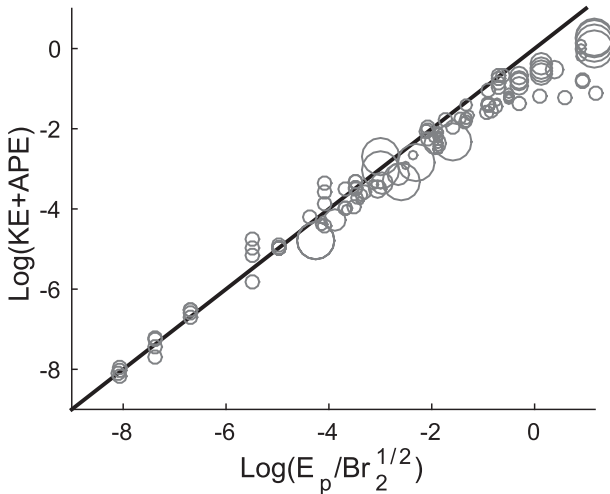
FIG. 5. The energy parameter $\hat{E}_p$ (gray circles) and the 1:1 line for reference. The size of the circle scales linearly with the Burger number; big circles indicate large Burger numbers (small storms).

removes APE through damping thickness perturbations in each layer. Each of the 11 nondimensional parameters was varied individually across a range of observation-based values when possible. Extreme cases (e.g., a storm areal fraction a_r as high as 40%) were simulated to test efficacy of the energy parameter. Empirically, the energy density in a given simulation appears to strongly affect its equilibrium behavior, and it is desirable to predict the energy density based on control parameters. Increasing the size, number, strength, or duration of the baroclinic storm forcing consistently results in a higher likelihood of a large-scale equivalent-barotropic cyclone in the domain. An increase in the storm frequency or the radiative time scale is also conducive to a polar cyclone.

Statistically steady states of the forced-dissipative models exhibit a broad spectrum of behavior, from very low-energy wave- and jet-dominated domains to very intense polar cyclones. OEF find that these states are controlled principally by two control quantities: the strength of a nondimensional beta parameter $\tilde{\beta}$ (which is proportional to the inverse of a/L_{D2}) and the energy density $\hat{E}_p$ due to convection of the shallow atmosphere. This energy parameter does a good job of capturing forced-dissipative simulation energy density, and here we further modify it for a better fit to the simulations.

In the case of the freely evolving single storms, there is no imposed radiative relaxation, and the forcing is only pulsed once in the beginning. For a constantly forced domain, energy is constantly injected and removed. We modify Eq. (11) by two corresponding time scales. A longer radiative time scale $\tilde{\tau}_{\mathrm{rad}}$ will remove energy more

slowly; and a longer period between storms $\tilde{\tau}_{\mathrm{stper}}$ will add energy more slowly. Thus, in the forced-dissipative case, we update our energy scale $\hat{E}_p = \hat{E}_p \tilde{\tau}_{\mathrm{rad}}/\tilde{\tau}_{\mathrm{stper}}$.

For the freely evolving cases above, in which a single storm is briefly forced in otherwise equal-thickness layers, it is appropriate to consider the contribution of APE due to subsidence as well as the storm itself. Since each round of storms (they are introduced in sets) is randomly placed, subsidence tends to damp locations that previously held small storms. Simulations with large a_r corroborate this, and we can therefore neglect the $(1 - a_r)$ factor in Eq. (11). Additionally, the square root of the Burger number, $\mathrm{Br}_2^{1/2} = L_{D2}/R_{\mathrm{st}}$, provides a marginally better match to the measured energy density of the forced-dissipative simulations than just the Burger number. These modifications slightly improve the energy parameter reported in EOF.

Our new energy parameter is

$$\hat{E}_p = \left(\frac{1}{2}\frac{\rho_1}{\rho_2}\tilde{c}_1^2 + \frac{1}{2}\frac{H_1}{H_2}\tilde{c}_2^2 - \gamma\tilde{c}_1^2\right)\frac{H_1}{H_2}(\mathrm{Ro}_{\mathrm{conv}}\tilde{\tau}_{\mathrm{st}})^2\frac{\tilde{\tau}_{\mathrm{rad}}}{\tilde{\tau}_{\mathrm{stper}}}\frac{a_r}{\sqrt{\mathrm{Br}_2}}.$$

(12)

The various regimes cannot be completely flattened to two dimensions. This is apparent, for example, when we change ρ_1/ρ_2 or H_1/H_2 by 50%. However, for nominal values of the control parameters, the outcome is quite predictable. The resulting $\hat{E}_p$ gives a reasonable estimate of the energy density in steady state for scores of simulations (Fig. 5). In Fig. 6, a subset of simulations is depicted where only 2 of the 11 control parameters are varied: $\tilde{\beta}$ and $\hat{E}_p$. Other parameters are held constant ($\tilde{c}_1^2 = 4$, $\tilde{c}_2^2 = 3$, $H_1/H_2 = 1$, $\mathrm{Br}_2 = 1$, $\rho_1/\rho_2 = 0.95$, $\tilde{\tau}_{\mathrm{st}} = 6$, $\tilde{\tau}_{\mathrm{stper}} = 15$, $\tilde{\tau}_{\mathrm{rad}} = 2000$, and $a_r = 15\%$). These simulations exhibit a representative range of behaviors.

a. Large $\tilde{\beta}$ (low a/L_{D2}) planets

Low-$\hat{E}_p$ simulations are wavelike, with multiple very weak jets. As $\hat{E}_p$ is increased, cyclonic eddies move poleward and a broad, transient region of positive perturbation PV collects on the pole, possibly similar to the transient polar hotspots observed on Neptune. As $\hat{E}_p$ is further increased, the transient region becomes much stronger and more symmetric. Low-a/L_{D2}, moderate-$\hat{E}_p$ planets most closely resemble polar observations of Saturn. Finally, more energy causes the polar cyclone to orbit/precess at greater distances from the pole. In the bottom row of Fig. 6, note that the most energetic/rightmost simulation has a polar vortex with a very tight circulation (the mean wind peaks close to center of vortex, shown by the dashed line). However, because of the relatively large distance of the vortex's center from the pole (gray line), the pole-centered mean winds are
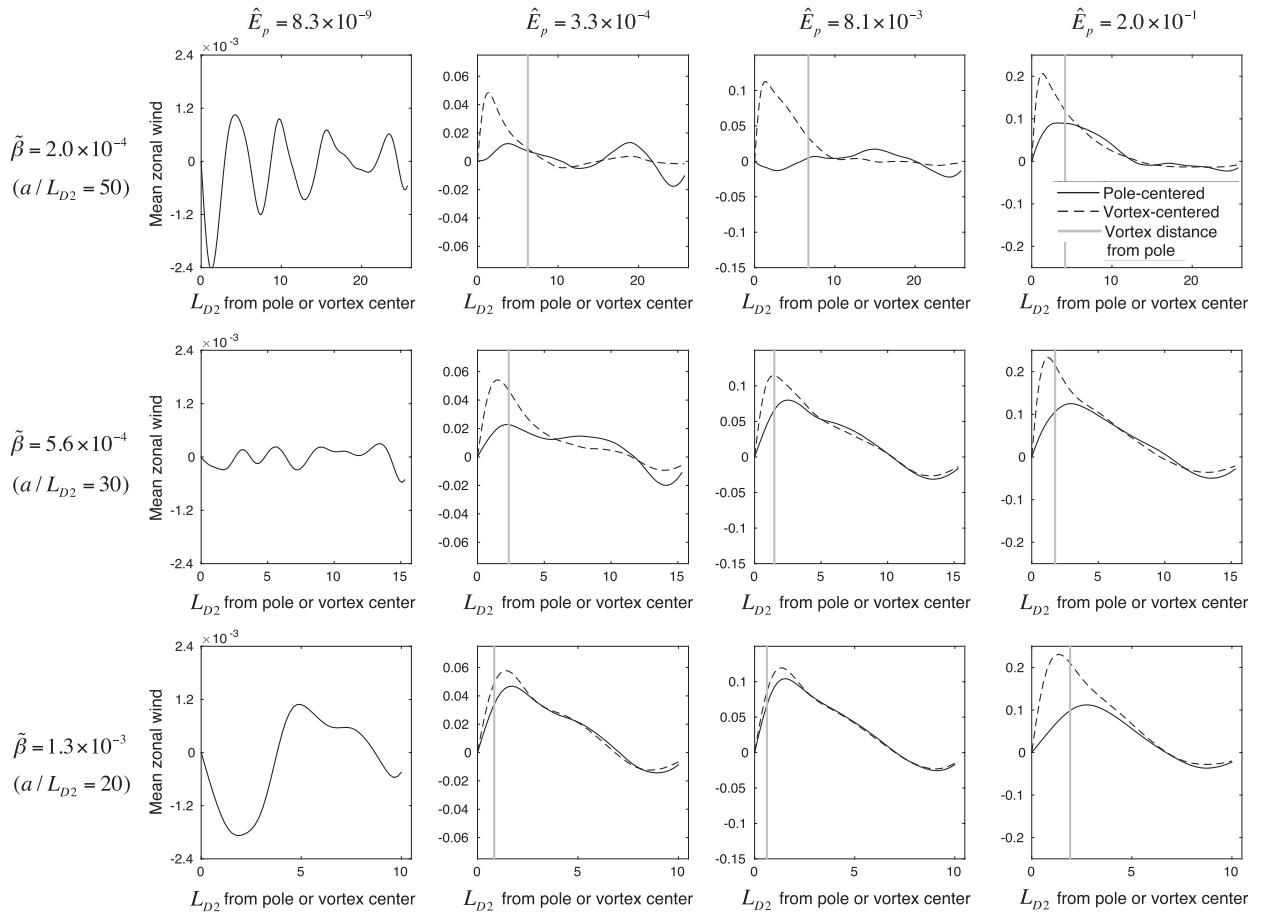
FIG. 6. Nondimensional mean zonal winds are shown for a range of planet sizes $\tilde{\beta}$ and energies $\hat{E}_p$ (changing Ro_{conv} as a proxy). Zonal winds are shown both with respect to the pole (solid lines) and with respect to the dominant cyclone center (dashed lines). (bottom)–(top) The effective Coriolis parameter decreases, and (left)–(right) energy increases. Vortex-centered profiles are not provided for the left column because these simulations do not produce a dominant vortex.

smeared in the time averaging and appear much weaker (black line).

b. Small $\tilde{\beta}$ (high a/L_{D2}) planets

A much weaker effective Coriolis gradient allows initially wavelike behavior to create and then merge multiple coherent vortices away from the pole as $\hat{E}_p$ is increased. Beyond the short deformation radius, a limited range of interaction and weakly nonlinear beta drift keeps low-energy behavior local. Stronger forcing can cause one or more strong circumpolar cyclones, but they will not be stable near the pole, instead directly transitioning to a polar orbit or nearly random motion.

WEAK JETS AND STRONG CYCLONES

The strong polar cyclone is by far the most dramatic outcome of the parameter sweep across a/L_{D2} and $\hat{E}_p$. However, in weakly energetic atmospheres, or on large $\tilde{\beta}$ planets, another persistent feature is very weak, increasingly equivalent-barotropic jets. These jets are initially fully baroclinic, in response to the purely baroclinic storm forcing. As time progresses, the jets ultimately align in the vertical. They are so weak as to be completely imperceptible in movies, as the wind field in these cases is dominated by small, storm-induced vortices. They can be seen quite clearly in a Hovmöller plot of polar radius and time (Fig. 7, top-left panel).

These weak jets may help us better understand observations of Jupiter's high latitudes (the poles themselves will be imaged for the first time in 2016, when the NASA *Juno* mission reaches Jupiter). While snapshots of Jupiter's high latitudes show an abundance of coherent cyclones and anticyclones, a movie[4] taken by *Cassini*'s narrow-angle camera over 70 days in 2000

---

[4] Available online at http://saturn.jpl.nasa.gov/video/videodetails/?videoID=224; credit: NASA/JPL/Southwest Research Institute.
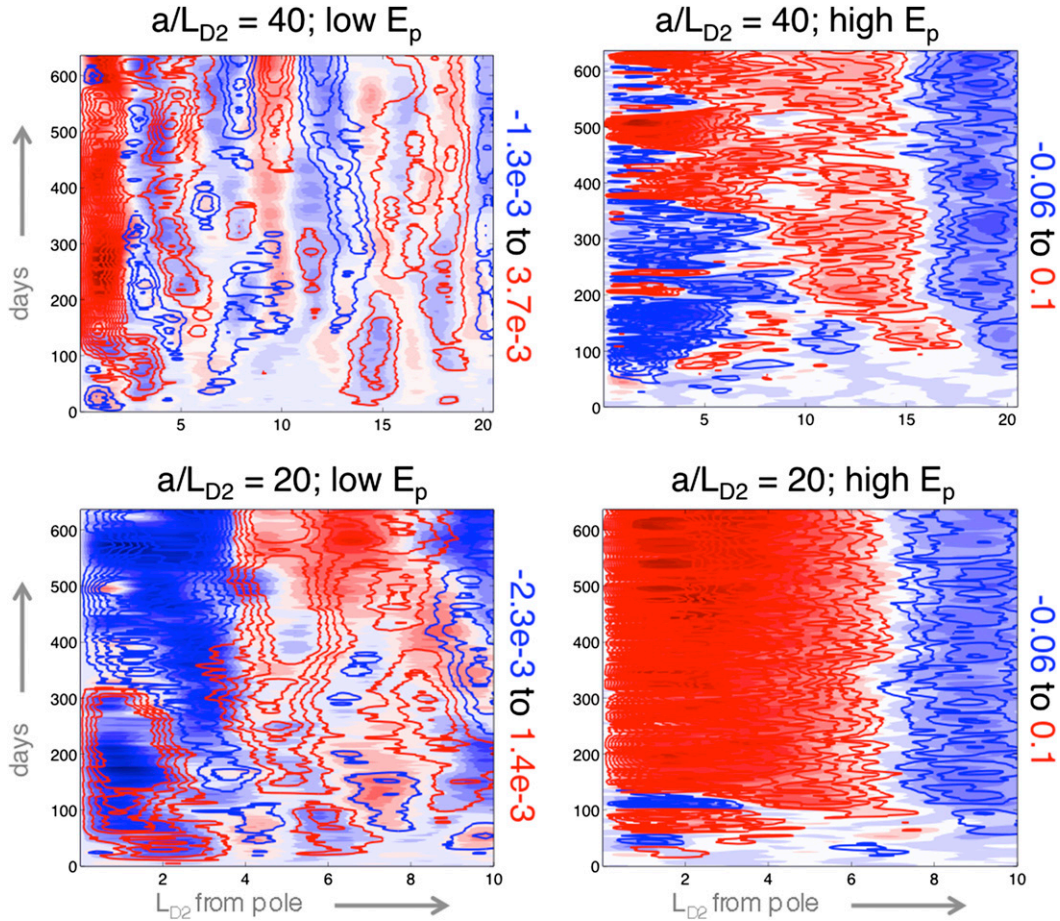
FIG. 7. Contours indicate nondimensional mean zonal winds in the upper layer; shading indicates nondimensional mean zonal winds in the lower layer. Maximum and minimum values are provided on the right-hand side of each panel. (top) Large planets relative to L_{D2}; (left) low $\hat{E}_p$ leads to multiple very weak jets, and (right) high $\hat{E}_p$ results in one or several strong cyclones that swim around in the polar region. (bottom) Small planets relative to L_{D2}; (left) low $\hat{E}_p$ leads to a couple broad and very weak jets, and (right) high $\hat{E}_p$ results in one strong cyclone that stays very close to the pole.

showed, surprisingly, that these vortices move zonally in very weak but well-defined narrow jets. This is similar to what is observed in the low-$\hat{E}_p$, high-a/L_{D2} simulations. Whether they are due to the same mechanism can be answered by a momentum flux convergence budget and comparison to pending detailed Jovian observations.

8. Discussion

A shallow-water model, customized for a polar cap that lacks a static bottom boundary, is able to achieve a strong, equivalent-barotropic polar cyclone under certain conditions. The model forcing emulates small, fast, energetic convective storms, and the radiative relaxation represents energy loss to space. The vortical hot tower mechanism of Montgomery et al. (2006) seems to be sufficient for cyclone spinup and maintenance.

This model is adequate for a study of horizontal shallow motions. Shortcomings in the shallow-water system and our geometry limit the applicability of our results to polar cyclones with Rossby number less than 1; for Rossby number much greater than 1, cyclostrophic vortices have vanishing layer depths. Both poles of Saturn appear to be depleted of phosphine gas, which varies as a function of both vertical mixing and photochemical destruction. This implies significant subsidence right at the poles (Fletcher et al. 2008), so we should seek a model that would permit this. The shallow-water model does not permit overturning circulations, though it can parameterize an overturning circulation through radiative relaxation. However, understanding whether that proxy is physically relevant or unphysically imposed remains to be seen in this case. Additionally, the most energetic simulations exhibit a peculiar instability, in

which the strongest cyclone spontaneously switches layers, leaving a weaker and annulus-shaped vortex in the former layer. Understanding and characterizing this instability is left for future work, and results for these extreme cases are not shown in this paper.

While our most stable polar cyclones are similar to those of Saturn, there is one major difference. Saturn's polar cyclones have never been observed away from their positions exactly over the poles, though admittedly the observations are extremely sparse by terrestrial standards. In the present simulations, no polar cyclone has been simulated that is as stationary. The most stable cyclones still wobble slightly over the pole, though they stray no farther than $1L_{D2}$ radially. Perhaps, on Saturn, there is a complex coupling between a fully developed weather-layer cyclone and the interior below. For example, if the forcing is large enough, it may spin up an equivalent-barotropic cyclone in the dry interior below that acts to stabilize the lateral motion of the weather-layer cyclone.

Interaction of the deep interior convection with the upper weather layer on giant planets is very unconstrained and an active area of research. It is commonly assumed that the interior just below the water cloud is fully convective and therefore adiabatic (e.g., Achterberg and Ingersoll 1989; Li and Ingersoll 2015). However, plume structures may allow local static stability (Lindzen 1977), and tidal forcing considerations suggest that below the cloud deck Jupiter may be (slightly) stably stratified (Ioannou and Lindzen 1994)[5]. This will affect the interpretation of our results. We assume that the deep interior is neutrally stable, which precludes a deformation radius. The water cloud may act as a waveguide (Ingersoll and Kanamori 1994) only if the stratification changes rapidly below it, and the only in situ evidence we have[6] suggests that this may not be true (Showman and Ingersoll 1998) (assuming that Jupiter and Saturn have similar upper stratifications).

We additionally assume that there is sufficient heat available in the lower layer to induce mass convergence and therefore cyclonic vorticity anomalies. On giant planets, it is unlikely that insolation reaches the lower troposphere, so the source of heat must be from the hot interior fluid. However, warming by the interior likely involves entrainment of interior parcels into the lower troposphere (our lower layer). In this work we do not include any mass exchange between the troposphere and the abyssal layer and instead assume that implicit mass exchange at the lower layer–abyss interface induces convergence as warmed, unstable weather-layer parcels rise convectively. It would be interesting to explore this assumption with a plume model—it is possible that the entrainment of moist tropospheric air that we assume here is insufficient to drive sufficient horizontal convergence. In this case, the divergence at upper levels would be greater than the lower-layer convergence, since some of the mass originated in the interior. Experiments in which H_1/H_2 was varied explored the possibility of a deep lower layer to emulate a very gradual transition to the neutral interior. These experiments, in which the lower layer was at least twice as thick as the upper layer, consistently developed a polar cyclone under similar conditions to the other simulations. This is despite a much lower maximum amplitude of lower-layer cyclonic vorticity compared to the anticyclonic vorticity above.

If we did include abyssal mass input, we would also include abyssal mass removal—just as in our two-layer exchange, these would result in sources of anticyclonic and cyclonic PV, respectively. This suggests an important role for downdrafts as a source of cyclonic PV, in the event that lower-layer convergence is negligible. This is an intriguing possibility because of the difficulty in motivating lower-layer convergence without a frictional boundary layer. Such a model would effectively be 1.5 layers, as in S07.

If the interior just below the weather layer is, in fact, statically stable, the present 2.5-layer model can be interpreted very differently. The upper layer can represent the entire weather layer; the lower layer can represent the upper, slightly stratified portion of the deep interior; and the abyssal layer can represent an even deeper neutral region. Under this interpretation, the first (external) baroclinic radius is actually the barotropic mode of the weather layer. The model's second baroclinic radius would then be the weather layer's *external* mode.

This would address one shortcoming of our results: a factor-of-almost-2 difference between Saturn's observed weather-layer deformation radius [1000–1500 km for the first baroclinic mode (Read et al. 2009)] and the simulated L_{D2} that produces qualitatively similar polar behavior, which is in the 1800–2800-km range. A first baroclinic deformation radius L_{D1} in our model is generally twice L_{D2}, which would be up to 4 times larger than estimates for Saturn. However, in our alternate interpretation above, it is possible that our L_{D2} actually acts like a first baroclinic mode, in which case the simulations are just a factor of 2 different than observational estimates.

---

[5] There may even be a radiative zone just below the weather layer, which would require an entire reassessment of our abyssal-layer assumptions (Guillot et al. 1994).

[6] The *Galileo* probe unfortunately pierced a "hot spot," which is likely quite anomalous (Niemann et al. 1998).

Saturn's polar cyclones have a peak in radial velocity approximately 3000 km from the pole. For our most Saturn-like simulations (Fig. 6, third column, middle and bottom rows), the radius of maximum winds is $2L_{D2}$ from the vortex center. For the lower end of simulated L_{D2} values that produce a relatively stable polar cyclone, this is roughly the same size as the real cyclones. Perhaps there is some merit to the second interpretation? Because there is very little theoretical understanding of the transition from the troposphere to the interior, and because the deformation radius estimates also cannot benefit from more vertical sounding data, for now this is the realm of speculation. Also, given the large number of poorly constrained free parameters (layer gravity wave speeds, convective storm abundance, etc.), it is difficult to tell whether we are in the right ballpark for $\hat{E}_p$, even as we use observationally motivated values for each parameter whenever possible.

OEF predict that, if polar cyclones are indeed shallow features, and if measurements of Saturn's and Jupiter's Rossby radii are sufficiently accurate, then NASA's *Juno* mission may not observe polar cyclones on Jupiter—at least not ones of comparable strength and stability to those on Saturn. Another testable component of our theory is a cold temperature anomaly near the bottom of the troposphere, consistent with the warm upper troposphere and the equivalent-barotropic PV structure of the cyclone.

APPENDIX A

Energy Equations

To derive nondimensional energy equations, multiply the upper-layer momentum equation by $(\rho_1/\rho_2)(H_1/H_2)h_1\mathbf{u}_1$ and the lower-layer momentum equation by $h_2\mathbf{u}_2$. Likewise, the upper mass conservation equation is multiplied by $(1/2)(\rho_1/\rho_2)(H_1/H_2)|\mathbf{u}_1|^2$; and the lower mass conservation equation is multiplied by $(1/2)|\mathbf{u}_2|^2$.

Expressions for layer kinetic and potential energy conservation are, respectively,

$$\frac{\partial K_1}{\partial t} = -\nabla \cdot \left(h_1 \mathbf{u}_1 \frac{1}{2} \frac{\rho_1}{\rho_2} \frac{H_1}{H_2} |\mathbf{u}_1|^2 \right)$$
$$+ \mathbf{u}_1 h_1 \cdot \nabla \left(\frac{1}{2} \frac{\rho_1}{\rho_2} \frac{H_1}{H_2} |\mathbf{u}_1|^2 \right) - \frac{\rho_1}{\rho_2} \frac{H_1}{H_2} h_1 \mathbf{u}_1 \mathrm{Re}^{-1} \nabla^4 \mathbf{u}_1, \quad (A1)$$

$$\frac{\partial K_2}{\partial t} = -\nabla \cdot \left(h_2 \mathbf{u}_2 \frac{1}{2} |\mathbf{u}_2|^2 \right)$$
$$+ \mathbf{u}_2 h_2 \cdot \nabla \left(\frac{1}{2} |\mathbf{u}_2|^2 \right) - h_2 \mathbf{u}_2 \mathrm{Re}^{-1} \nabla^4 \mathbf{u}_2, \quad (A2)$$

$$\frac{\partial P_1}{\partial t} = -\nabla \cdot \left[h_1 \mathbf{u}_1 \frac{\rho_1}{\rho_2} \frac{H_1}{H_2} (\tilde{c}_1^2 h_1 + \tilde{c}_2^2 h_2) \right]$$
$$- \mathbf{u}_1 h_1 \cdot \nabla \left(\frac{1}{2} \frac{\rho_1}{\rho_2} \frac{H_1}{H_2} |\mathbf{u}_1|^2 \right)$$
$$+ \frac{1}{2} \frac{\rho_1}{\rho_2} \frac{H_1}{H_2} |\mathbf{u}_1|^2 \left(S_{\mathrm{st}} - \frac{h_1 - 1}{\tilde{\tau}_{\mathrm{rad}}} + \mathrm{Pe}^{-1} \nabla^2 h_1 \right), \quad (A3)$$

$$\frac{\partial P_2}{\partial t} = -\nabla \cdot [h_2 \mathbf{u}_2 (\gamma \tilde{c}_1^2 h_1 + \tilde{c}_2^2 h_2)] - \mathbf{u}_2 h_2 \cdot \nabla \left(\frac{1}{2} |\mathbf{u}_2|^2 \right)$$
$$+ \frac{1}{2} |\mathbf{u}_2|^2 \left(\frac{H_1}{H_2} S_{\mathrm{st}} - \frac{h_2 - 1}{\tilde{\tau}_{\mathrm{rad}}} + \mathrm{Pe}^{-1} \nabla^2 h_2 \right), \quad (A4)$$

where total kinetic energy K, total potential energy P (to some constant), and total available potential energy A are, respectively,

$$K = \frac{1}{2} \left(\frac{\rho_1}{\rho_2} \frac{H_1}{H_2} h_1 |\mathbf{u}_1|^2 + h_2 |\mathbf{u}_2|^2 \right), \quad (A5)$$

$$P = \frac{1}{2} \frac{\rho_1}{\rho_2} \frac{H_1}{H_2} \tilde{c}_1^2 h_1^2 + \frac{1}{2} \tilde{c}_2^2 h_2^2 + \gamma \tilde{c}_1^2 h_1 h_2, \quad (A6)$$

$$A = \frac{1}{2} \frac{\rho_1}{\rho_2} \frac{H_1}{H_2} \tilde{c}_1^2 h_1'^2 + \frac{1}{2} \tilde{c}_2^2 h_2'^2 + \gamma \tilde{c}_1^2 h_1' h_2'. \quad (A7)$$

It can be shown that while the final term on the rhs of the expression for A is often negative, total A is always positive, as we expect.

APPENDIX B

Numerical Considerations

As in OEF (methods section), the Cartesian grid is a staggered Arakawa C grid. The time-stepping scheme is a second-order Adams–Bashforth algorithm. Early tests showed that this provided dynamics nearly identical to the third-order Adams–Bashforth scheme. Horizontal hyperviscosity ∇^4 is used instead of viscosity to reduce its impact on the dynamics, which at upper levels on giant planets is virtually inviscid. The Reynolds and Peclet numbers are fixed at the highest values that

empirically permit consistent numerical stability (5×10^4 and 1×10^5, respectively), so we explore an 11-dimensional parameter space. For all simulations, we impose a resolution constraint on the second baroclinic deformation radius of $L_{D2} = 5dx$ in order to consistently resolve filamentation and enstrophy for a wavelength smaller than L_{D2}.

Domain

The domain is doubly periodic, which allows us to prevent corner effects, but it causes a discontinuity in the Coriolis gradient β at the open boundaries. To mitigate the possibility of features leaving and reentering the domain at opposite longitudes, we impose an azimuthally symmetric sponge layer[B1] at each time step. This sponge layer is a simple Rayleigh damping term, and the damping time scale decreases linearly from infinity to 0.8 days with radius. For domain size L^2, the sponge layer generally begins at radius $L/2 - 0.5L_{D2}$ for a second baroclinic deformation radius L_{D2}. This sponge layer acts too slowly to absorb fast gravity waves. However, in the parameter space of interest, storms develop relatively slowly and so gravity waves are not strongly excited.

An observational estimate for Saturn's first deformation radius in the polar region is 1000–1500 km (Read et al. 2009), or around one-tenth of the distance to the first jet. For Jupiter, an estimated first deformation radius is 1000 km or less (Read et al. 2006). In this model, the planet size is scaled by the *second* deformation radius L_{D2}, because it is the dominant mode of moist convection and, unlike L_{D1}, is resolved consistently. A drawback of comparing simulation results to observed deformation radii is that the observations likely measure a first-baroclinic deformation radius, though without in situ measurements it is hard to know for sure. We set a benchmark domain size $L_{\text{dom}}^2 = a^2$, and the radial extent for most simulations is $a/2$, or about 30° from the pole. The polar beta plane is a very good approximation over this entire domain.

The difficulty arises when considering the ice giants Uranus and Neptune, because their deformation radius is estimated to be up to one-third of their planetary radius (Polvani et al. 1990). Most simulations in this work resolve L_{D2} by five grid points. If we tried to simulate a

planet with $a/L_{D2} = 3$, the limit of polar beta-plane validity would be reached within those five grid points—certainly an absurd proposition. In these simulations, the range of a/L_{D2} examined is 20–70.

REFERENCES

Achterberg, R. K., and A. P. Ingersoll, 1989: A normal-mode approach to Jovian atmospheric dynamics. *J. Atmos. Sci.*, **46**, 2448–2462, doi:10.1175/1520-0469(1989)046<2448:ANMATJ>2.0.CO;2.

Adem, J., 1956: A series solution for the barotropic vorticity equation and its application in the study of atmospheric vortices. *Tellus*, **8A**, 364–372, doi:10.1111/j.2153-3490.1956.tb01234.x.

Baines, K. H., and Coauthors, 2009: Saturn's north polar cyclone and hexagon at depth revealed by *Cassini*/VIMS. *Planet. Space Sci.*, **57**, 1671–1681, doi:10.1016/j.pss.2009.06.026.

Bridger, A. F. C., and D. E. Stevens, 1980: Long atmospheric waves and the polar-plane approximation to the earth's spherical geometry. *J. Atmos. Sci.*, **37**, 534–544, doi:10.1175/1520-0469(1980)037⟨0534:LAWATP⟩2.0.CO;2.

Chan, J. C. L., and R. T. Williams, 1987: Analytical and numerical studies of the beta-effect in tropical cyclone motion. Part I: Zero mean flow. *J. Atmos. Sci.*, **44**, 1257–1265, doi:10.1175/1520-0469(1987)044<1257:AANSOT>2.0.CO;2.

Conrath, B. J., P. J. Gierasch, and S. S. Leroy, 1990: Temperature and circulation in the stratosphere of the outer planets. *Icarus*, **83**, 255–281, doi:10.1016/0019-1035(90)90068-K.

Dritschel, D. G., and M. E. Mcintyre, 2008: Multiple jets as PV staircases: The Phillips effect and the resilience of eddy-transport barriers. *J. Atmos. Sci.*, **65**, 855–874, doi:10.1175/2007JAS2227.1.

Dyudina, U. A., and Coauthors, 2009: Saturn's south polar vortex compared to other large vortices in the solar system. *Icarus*, **202**, 240–248, doi:10.1016/j.icarus.2009.02.014.

Emanuel, K. A., 1986: An air–sea interaction theory for tropical cyclones. Part I: Steady-state maintenance. *J. Atmos. Sci.*, **43**, 585–605, doi:10.1175/1520-0469(1986)043<0585:AASITF>2.0.CO;2.

Fletcher, L. N., and Coauthors, 2008: Temperature and composition of Saturn's polar hot spots and hexagon. *Science*, **319**, 79–81, doi:10.1126/science.1149514.

——, and Coauthors, 2015: Seasonal evolution of Saturn's polar temperatures and composition. *Icarus*, **250**, 131–153, doi:10.1016/j.icarus.2014.11.022.

Flierl, G. R., 1984: Rossby wave radiation from a strongly nonlinear warm eddy. *J. Phys. Oceanogr.*, **14**, 47–58, doi:10.1175/1520-0485(1984)014<0047:RWRFAS>2.0.CO;2.

Gierasch, P. J., and Coauthors, 2000: Observation of moist convection in Jupiter's atmosphere. *Nature*, **403**, 628–630, doi:10.1038/35001017.

Guillot, T., D. Gautier, G. Chabrier, and B. Mosser, 1994: Are the giant planets fully convective? *Icarus*, **112**, 337–353, doi:10.1006/icar.1994.1188.

Hendricks, E. A., W. H. Schubert, Y.-H. Chen, H.-C. Kuo, and M. S. Peng, 2014: Hurricane eyewall evolution in a forced shallow-water model. *J. Atmos. Sci.*, **71**, 1623–1643, doi:10.1175/JAS-D-13-0303.1.

Ingersoll, A. P., and H. Kanamori, 1994: Waves from the collisions of comet Shoemaker–Levy 9 with Jupiter. *Nature*, **374**, 706–708, doi:10.1038/374706a0.

——, and Coauthors, 2000: Moist convection as an energy source for the large-scale motions in Jupiter's atmosphere. *Nature*, **403**, 630–632, doi:10.1038/35001021.

[B1] The sponge layer is not responsible for containing a medium-energy cyclone near the pole. If it were, this would be a significant deficiency of the model. A simulation run in the current version of the model, without a sponge layer, also creates a polar cyclone. The major difference was that the total energy increases linearly for the duration of the integration, while the corresponding model with a sponge layer is able to reach statistical energy equilibrium well before. Scores of simulations run in a previous version of the model, before the sponge-layer implementation, confirm the same result.

Ioannou, P. J., and R. S. Lindzen, 1994: Gravitational tides on Jupiter. 3: Atmospheric response and mean flow acceleration. *Astrophys. J.*, **424**, 1005–1013, doi:10.1086/173951.

Kaspi, Y., G. R. Flierl, and A. P. Showman, 2009: The deep wind structure of the giant planets: Results from an anelastic general circulation model. *Icarus*, **202**, 525–542, doi:10.1016/j.icarus.2009.03.026.

Leblond, P. H., 1964: Planetary waves in a symmetrical polar basin. *Tellus*, **16A**, 503–512, doi:10.1111/j.2153-3490.1964.tb00185.x.

Li, C., and A. P. Ingersoll, 2015: Moist convection in hydrogen atmospheres and the frequency of Saturn's giant storms. *Nature Geosci.*, **8**, 398–403, doi:10.1038/ngeo2405.

Li, L., A. P. Ingersoll, A. R. Vasavada, C. C. Porco, A. D. D. Genio, and S. P. Ewald, 2004: Life cycles of spots on Jupiter from *Cassini* images. *Icarus*, **172**, 9–23, doi:10.1016/j.icarus.2003.10.015.

Lian, Y., and A. P. Showman, 2010: Generation of equatorial jets by large-scale latent heating on the giant planets. *Icarus*, **207**, 373–393, doi:10.1016/j.icarus.2009.10.006.

Lindzen, R. S., 1977: Some aspects of convection in meteorology. *Problems of Stellar Convection*, E. A. Spiegel and J.-P. Zahn, Eds., Lecture Notes in Physics, Vol. 71, Springer-Verlag, 128–141, doi:10.1007/3-540-08532-7_38.

Little, B., and Coauthors, 1999: Galileo images of lightning on Jupiter. *Icarus*, **142**, 306–323, doi:10.1006/icar.1999.6195.

Liu, J., and T. Schneider, 2010: Mechanisms of jet formation on the giant planets. *J. Atmos. Sci.*, **67**, 3652–3672, doi:10.1175/2010JAS3492.1.

——, and ——, 2011: Convective generation of equatorial superrotation in planetary atmospheres. *J. Atmos. Sci.*, **68**, 2742–2756, doi:10.1175/JAS-D-10-05013.1.

McWilliams, J. C., L. P. Graves, and M. T. Montgomery, 2003: A formal theory for vortex Rossby waves and vortex evolution. *Geophys. Astrophys. Fluid Dyn.*, **97**, 275–309, doi:10.1080/0309192031000108698.

Melander, M. V., J. C. McWilliams, and N. J. Zabusky, 1987: Axisymmetrization and vorticity-gradient intensification of an isolated two-dimensional vortex through filamentation. *J. Fluid Mech.*, **178**, 137–159, doi:10.1017/S0022112087001150.

Möller, J. D., and M. T. Montgomery, 1999: Vortex rossby waves and hurricane intensification in a barotropic model. *J. Atmos. Sci.*, **56**, 1674–1687, doi:10.1175/1520-0469(1999)056<1674:VRWAHI>2.0.CO;2.

Montgomery, M. T., and R. J. Kallenbach, 1997: A theory for vortex Rossby-waves and its application to spiral bands and intensity changes in hurricanes. *Quart. J. Roy. Meteor. Soc.*, **123**, 435–465, doi:10.1002/qj.49712353810.

——, M. E. Nicholls, T. A. Cram, and A. B. Saunders, 2006: A vortical hot tower route to tropical cyclogenesis. *J. Atmos. Sci.*, **63**, 355–386, doi:10.1175/JAS3604.1.

Niemann, H. B., and Coauthors, 1998: The composition of the Jovian atmosphere as determined by the Galileo probe mass spectrometer. *J. Geophys. Res.*, **103**, 22 831–22 845, doi:10.1029/98JE01050.

Nolan, D. S., and L. D. Grasso, 2003: Nonhydrostatic, three-dimensional perturbations to balanced, hurricane-like vortices. Part II: Symmetric response and nonlinear simulations. *J. Atmos. Sci.*, **60**, 2717–2745, doi:10.1175/1520-0469(2003)060<2717:NTPTBH>2.0.CO;2.

O'Neill, M. E, 2015: A theory for polar cyclones on giant planets. Ph.D. thesis, Massachusetts Institute of Technology, 145 pp. [Available online at http://hdl.handle.net/1721.1/97335.]

——, K. A. Emanuel, and G. R. Flierl, 2015: Polar vortex formation in giant-planet atmospheres due to moist convection. *Nature Geosci.*, **8**, 523–526, doi:10.1038/ngeo2459.

Orton, G. S., and P. A. Yanamandra-Fisher, 2005: Saturn's temperature field from high-resolution middle-infrared imaging. *Science*, **307**, 696–698, doi:10.1126/science.1105730.

Persing, J., M. T. Montgomery, J. C. McWilliams, and R. K. Smith, 2013: Asymmetric and axisymmetric dynamics of tropical cyclones. *Atmos. Chem. Phys.*, **13**, 12 299–12 341, doi:10.5194/acp-13-12299-2013.

Polvani, L. M., 1991: Two-layer geostrophic vortex dynamics. Part 2. Alignment and two-layer V-states. *J. Fluid Mech.*, **225**, 241–270, doi:10.1017/S0022112091002045.

——, J. Wisdom, E. DeJong, and A. P. Ingersoll, 1990: Simple dynamical models of Neptune's great dark spot. *Science*, **249**, 1393–1398, doi:10.1126/science.249.4975.1393.

Read, P. L., P. J. Gierasch, B. J. Conrath, A. Simon-Miller, T. Fouchet, and Y. H. Yamazaki, 2006: Mapping potential-vorticity dynamics on Jupiter. I: Zonal-mean circulation from Cassini and Voyager 1 data. *Quart. J. Roy. Meteor. Soc.*, **132**, 1577–1603, doi:10.1256/qj.05.34.

——, B. Conrath, L. Fletcher, P. Gierasch, A. Simon-Miller, and L. Zuchowski, 2009: Mapping potential vorticity dynamics on Saturn: Zonal mean circulation from *Cassini* and Voyager data. *Planet. Space Sci.*, **57**, 1682–1698, doi:10.1016/j.pss.2009.03.004.

Sánchez-Lavega, A., R. Hueso, S. Pérez-Hoyos, and J. F. Rojas, 2006: A strong vortex in Saturn's south pole. *Icarus*, **184**, 524–531, doi:10.1016/j.icarus.2006.05.020.

Schecter, D. A., and D. H. E. Dubin, 1999: Vortex motion driven by a background vorticity gradient. *Phys. Rev. Lett.*, **83**, 2191–2194, doi:10.1103/PhysRevLett.83.2191.

Schneider, T., and J. Liu, 2009: Formation of jets and equatorial superrotation on Jupiter. *J. Atmos. Sci.*, **66**, 579–601, doi:10.1175/2008JAS2798.1.

Scott, R. K., 2011: Polar accumulation of cyclonic vorticity. *Geophys. Astrophys. Fluid Dyn.*, **105**, 409–420, doi:10.1080/03091929.2010.509927.

——, and L. M. Polvani, 2007: Forced-dissipative shallow-water turbulence on the sphere and the atmospheric circulation of the giant planets. *J. Atmos. Sci.*, **64**, 3158–3176, doi:10.1175/JAS4003.1.

——, and ——, 2008: Equatorial superrotation in shallow atmospheres. *Geophys. Res. Lett.*, **35**, L24202, doi:10.1029/2008GL036060.

Showman, A. P., 2007: Numerical simulations of forced shallow-water turbulence: Effects of moist convection on the large-scale circulation of Jupiter and Saturn. *J. Atmos. Sci.*, **64**, 3132–3157, doi:10.1175/JAS4007.1.

——, and A. P. Ingersoll, 1998: Interpretation of Galileo probe data and implications for Jupiter's dry downdrafts. *Icarus*, **132**, 205–220, doi:10.1006/icar.1998.5898.

Simonnet, E., M. Ghil, K. Ide, R. Temam, and S. Wang, 2003: Low-frequency variability in shallow-water models of the wind-driven ocean circulation. Part I: Steady-state solution. *J. Phys. Oceanogr.*, **33**, 712–728, doi:10.1175/1520-0485(2003)33<712:LVISMO>2.0.CO;2.

Smith, K. S., 2004: A local model for planetary atmospheres forced by small-scale convection. *J. Atmos. Sci.*, **61**, 1420–1433, doi:10.1175/1520-0469(2004)061<1420:ALMFPA>2.0.CO;2.

Vasavada, A. R., S. M. Hörst, M. R. Kennedy, A. P. Ingersoll, C. C. Porco, A. D. Del Genio, and R. A. West, 2006: *Cassini* imaging of Saturn: Southern hemisphere winds and vortices. *J. Geophys. Res.*, **111**, E05004, doi:10.1029/2005JE002563.

Venaille, A., G. K. Vallis, and S. M. Griffies, 2012: The catalytic role of the beta effect in barotropization processes. *J. Fluid Mech.*, **709**, 490–515, doi:10.1017/jfm.2012.344.